Research Square

Preprints are preliminary reports that have not undergone peer review.
They should not be considered conclusive, used to inform clinical practice,
or referenced by the media as validated information.

Design of polyvinyl alcohol/bacterial cellulose/sodium alginate/MXene@Polydopamine hydrogel evaporator for fresh water acquisition

Lei Chen
Zhilong Lin
Yu Gao
Wenqin Wang
wangwenqin@nbu.edu.cn

Ningbo University https://orcid.org/0000-0002-2302-1467

Research Article

Keywords: Hydrogel, Photothermal evaporation, Fresh water acquisition, Sewage, Desalination

Posted Date: April 1st, 2026

DOI: https://doi.org/10.21203/rs.3.rs-9213109/v1

License: This work is licensed under a Creative Commons Attribution 4.0 International License.
Read Full License

Abstract

In this work, a stable physically crosslinked multi-network hydrogel was constructed using polyvinyl alcohol (PVA)/sodium alginate (SA) mixture as the backbone framework and bacterial cellulose (BC) nanofiber as “bridging agents.” MXene@Polydopamine (MXene@PDA) composites with high oxidation resistance and light-to-heat conversion ability as photothermal components were incorporated into above hydrogel networks to build a PVA/BC/SA/MXene@PDA photothermal evaporator. The as-obtained evaporator exhibited a high evaporation rate, good cyclic stability and salt tolerance. Consequently, this evaporator not only could harvest freshwater from dye sewage but also executed efficiently seawater desalination.

1. Introduction

Acquisition of fresh water from sewage and seawater is a proactive and effectual solution to alleviate a critical crisis of freshwater scarcity [1–3]. Currently, the solar-driven interfacial evaporation technology has developed rapidly because it abandons the defects (such as high energy consumption, substantial costs and environmental pollution) of traditional techniques [4–8]. To improve the efficiency of fresh water acquisition, the design of interfacial evaporators has been a key issue in the scientific and industrial field. In general, to a deal interfacial evaporator, a hydrophilic three-dimensional porous framework with ease of fabrication, high water transport efficiency as well as strong mechanical stability, and a photothermal material with excellent photo-thermal conversion ability are indispensable [9–11]. Among of various three-dimensional interfacial evaporators, polymer-based hydrogel evaporators have stood out for their exceptional hydrophilicity, tunable porous architecture, and environmental friendliness [12, 13]. Polyvinyl alcohol (PVA) containing abundant hydroxyl groups and sodium alginate (SA) containing lots of hydroxyl and carboxyl groups have been widely used to construct hydrophilic networks [14, 15]. MXene has also emerged as a promising photothermal material from numerous photothermal materials due to its broad-spectrum absorption and highly efficient photothermal conversion capabilities [16–18]. Integrating PVA/SA hydrogel with MXene to construct photothermal evaporators has been widely studied and exhibited enormous potential for purification of sewage and seawater desalination [19–21]

Despite their popularity, the PVA/SA/MXene evaporator still remain several shortcomings. For example, the mechanical properties of PVA/SA hydrogels do not entirely meet the requirements under some harsh conditions. So, the chemical crosslinking agents (such as metal salts) were usually required, whose residual metal ions may cause secondary harm to water bodies. The irreversible crosslinked network structure made it difficult to degrade and recycle discarded hydrogels [22–24]. MXene readily oxidizes and agglomerates, leading to uneven photothermal absorption and poor stability [25]. Additionally, the potential compatibility issue between PVA/SA and MXene also was concerned.

To address the aforementioned drawbacks, in this work, bacterial cellulose (BC) nanofibers were introduced into the conventional PVA/SA hydrogel to improve the mechanical performance of the

hydrogel. BC served as a “bridging” to connect PVA and SA, forming a more stable and stronger multi-network hydrogel owing to the large-scale introduction of hydrogen bonds [26]. To enhance the oxidation resistance of MXene, polydopamine (PDA) layer was covered on MXene, isolating water and oxygen from contacting MXene and while simultaneously avoiding the agglomeration of MXene [27, 28]. Besides these merits, the rich hydroxy groups of PDA enabled MXene@PDA composites to be toughly immobilized within the hydrogel by forming massive hydrogen bonding with hydrogel components. By the above strategies, the as-obtained hydrogel evaporator presented excellent photothermal evaporation performance, including high water evaporation rates, good salt tolerance and robust structural stability. This hydrogel evaporator also exhibited the practical potential of freshwater acquisition from sewage containing organic dye contaminants (methylene blue, methyl orange, and rhodamine B) and brine water.

2. Experimental section

2.1 Materials

Polyvinyl alcohol (PVA, 1799), hydrochloric acid (HCl, 36%), dopamine hydrochloride (DA-HCl, 98%) and tris(hydroxymethyl)aminomethane (Tris, 99%) were purchased from Sigma-Aldrich. Sodium alginate (SA, CP, 200 ± 20 mPa·s) and lithium fluoride (LiF, 99%) were purchased from Macklin Biochemical Technology Co., Ltd. Bacterial cellulose suspension (BC, 0.8 wt%) was purchased from Guilin Qixin Co., Ltd.; Titanium aluminum carbide (Ti_3AlC_2, 400 mesh, 98%) was purchased from Xinxi Technology Co., Ltd. Methylene blue (MB), Rhodamine B (RhB) and Methyl Orange (MO) were purchased from Shanghai Aladdin Reagent Co., Ltd. All chemical reagents were used directly without further purification.

2.2 Preparation of MXene@PDA composites

MXene nanosheets were prepared according to the previous report [19]. 50 mL of MXene suspension and 2.5 mL of tris buffer solution (20 mg/mL) were mixed and pH of the mixed solution was adjusted to 8.5. Subsequently, dopamine hydrochloride (DA-HCl) was added into above solution and the whole mixture was stirred at ambient temperature. After 24 h, the precipitate was collected by centrifuging and washing with deionized water for 2–3 cycles. Finally, the product (MXene@PDA composite) was freeze-dried for 48 h.

2.3 Preparation of P-BC-S/MXene@PDA hydrogels

30 mL of PVA solution (3 wt%) and 10 mL of BC suspension (0.8 wt%) were homogeneously mixed, defined as solution A. 10 mL of SA solution (2 wt%) and 10 mL of BC suspension (0.8 wt%) were uniformly mixed, defined as solution B. Subsequently, 25 mL of solution A, 10 mL of solution B and 5 mL of MXene@PDA suspension (3 wt%) were mixed thoroughly, and the resultant mixture was poured into a prefabricated mold. The mold was frozen at -20°C for 6 h and thawed at room temperature, and this freeze-thaw cycle was repeated 3 times to obtain the PVA/BC/SA/MXene@PDA composite hydrogel, named P-BC-S/MXene@PDA hydrogel.

2.4 Characterization of P-BC-S/MXene@PDA hydrogel

Scanning electron microscopy (SEM, Nova NanoSEM450) and transmission electron microscopy (TEM, Tecnai F20) were employed to observe the microstructure of the samples. Wetting properties of the samples were evaluated using a contact angle analyzer (CA, DSA 100S). Chemical composition analysis of the samples was performed with a Fourier transform infrared spectrometer (FTIR, Nicolet 6700), X-ray photoelectron spectroscopy (XPS, Axis Ultra DLD) and X-ray spectroscopy (EDS, Thermo Scientific). Phase composition was characterized using X-ray powder diffraction (XRD, BRUKER D8 advance). The evaporation enthalpy of the samples in water was measured using a differential scanning calorimeter (DSC, Nexi). The mechanical properties of the samples were evaluated using a universal tensile testing machine (ZwickRoll BUP 1000). The absorption spectra of the hydrogels between 200 nm and 2500 nm were analyzed using a UV-vis-IR spectrophotometer (Lambda 850+). The absorbance of the samples was measured by a UV-vis spectrophotometer (Lambda 850+). The concentration of metal ions in seawater and purified water was analyzed by an inductively coupled plasma optical emission spectrometer (ICP-OES, SPECTRO ARCOS).

3. Results and discussion

3.1 Preparation process of P-BC-S/MXene@PDA hydrogel

The preparation process of the P-B-S/MXene@PDA hydrogel is illustrated in Fig. 1. Ti_3AlC_2 precursor was etched by LiF/HCl to obtain multilayer $Ti_3C_2T_X$. After an ultrasonic dispersion process, the monolayer $Ti_3C_2T_X$ nanosheets were obtained. Under a weakly alkaline condition, DA performed a self-polymerization reaction and the surface of MXene nanosheets were covered by PDA. The MXene@PDA suspension was then added to the P-BC-S solution and the P-BC-S/MXene@PDA hydrogel was yielded by the repeated freeze-thaw cycles.

3.2 Characterization and antioxidant properties of MXene@PDA composites

The TEM image of MXene was exhibited in Fig. S1, confirming the successful preparation of MXene nanosheets [29]. XRD patterns of the relevant samples were shown in Fig. S2. After etching, the 38.8° (104) crystal plane diffraction peak of Ti_3AlC_2 disappeared, and the 9.5° (002) crystal plane diffraction peak shifted to 6.8°, indicating the entire exfoliation of Al layers. Compared with MXene, the crystal plane (002) of MXene@PDA composites shifted to 5.4°, hinting the successful surface modification of MXene with PDA. This result could be further demonstrated by the FTIR spectrum (Fig. S3). In FTIR spectrum of MXene@PDA composites, a characteristic peak at 1300 cm^{-2} attributed to C-N group of PDA was obviously observed [28]. The peak at 1679 cm^{-1} was corresponded to C = O groups, confirming the successful formation of a hydrogen-bond network on the MXene surface. The peaks at 865 cm^{-1} and 3457 cm^{-1} were attributed to PDA's phenolic hydroxyl groups and O-H stretching vibrations. PDA layer could effectively protect MXene from being oxidized. Digital images documenting the color evolution over time of MXene and MXene@PDA suspension stored at room temperature for 30 days were

presented in Fig. S4. The MXene dispersion initially exhibited a black color, and gradually faded after 30 days because of the progressive oxidation of MXene in the aqueous-oxygen environment. Conversely, MXene@PDA suspension basically maintained its original color, which might be explained that the dense PDA layer prevented direct contact between H_2O and O_2 with the MXene surface. Moreover, the plentiful phenol and quinone groups of PDA could capture and quench the reactive oxygen species within the system, effectively blocking the oxidative reaction targeting MXene [30].

3.3 Characterization of the P-BC-S/MXene@PDA hydrogel evaporator

The microstructure of hydrogel samples was characterized using SEM. In Fig. 2(a, a_1), the P-BC-S hydrogel revealed the multi-level interconnected network structure. As shown in Fig. 2(b, b_1), the P-BC-S/MXene@PDA hydrogel maintained the integrity of the porous framework. The encapsulation effect of PDA on MXene enhanced the surface roughness of the pore walls within the hydrogel. In the EDS spectrum of the P-BC-S/MXene@PDA hydrogel shown in Fig. 2c, the distribution of C elements corresponded to the three-dimensional network framework of the P-BC-S hydrogel and the carbon skeleton structure of the MXene@PDA composites. The uniform distribution of Ti and F elements confirmed that MXene@PDA composites were uniformly dispersed throughout the hydrogel. Wetting performances of the hydrogels were revealed in Fig. 2d. The P-BC-S hydrogel exhibited good hydrophilic performance due to the abundant -OH groups and porous structure. After introduction of MXene@PDA composites, the P-BC-S/MXene@PDA hydrogel still maintained excellent hydrophilicity, which was favorable for the water transport in solar interface evaporation process.

The full XPS spectra of the samples were shown in Fig. 2e. After in situ etching of MAX phase with LiF/HCl, MXene surface retained Ti-C (454.2 eV) bonds and the etching byproduct TiF_3 (459.8 eV) phase [31]. The PDA on MXene surface introduced -N= (398.2 eV) and -NH- (400.1 eV) bonds (Fig. S5a, b). The P-BC-S hydrogel exhibited two characteristic peaks in the C 1s region: C-C (284.8 eV) and C-O (286.3 eV), attributed to the carbon backbones of PVA, BC, and SA, as well as the hydroxyl groups of PVA and SA (Fig. S5c). Following the incorporation of MXene@PDA, the C 1s region showed broadened C-Ti (283.6 eV) and C-C (284.8 eV) peaks (Fig. S5d) [32]. These results undoubtedly confirmed the coexistence of MXene@PDA in the P-BC-S hydrogel.

The key to utilizing hydrogels as evaporators lies in harnessing their internal water confinement and regulating water's phase transition behavior to reduce evaporation enthalpy and enhance evaporation rates. DSC characterization of water evaporation enthalpy from hydrogels (Fig. 2f) revealed that water within the hydrogel could form “bound water” through hydrogen bonding interactions with PVA, BC and SA. This increased the proportion of activated water, leading to a decrease in the enthalpy of evaporation. The MXene@PDA composites could further enhance the interactions within the hydrogel network, resulting in a slightly higher enthalpy of evaporation, yet it remained significantly lower than that of pure water. In practical applications, the mechanical properties of hydrogel interfacial evaporators are particularly crucial. The mechanical performances of the hydrogels were evaluated through compression

testing. As shown in Fig. 2g, the mechanical performance of the P-BC-S/MXene@PDA hydrogel was more excellent than that of the P-BC-S hydrogel. The result could be attributed to the following reasons: (1) MXene@PDA composites served as an effective physical crosslinking point within the hydrogel network. (2) the abundant active functional groups (-OH and -NH_2 groups) on the MXene@PDA surface could form extensive hydrogen-bond networks with -OH groups of PVA, BC, and SA.

3.4 Photothermal conversion performance of the P-BC-S/MXene@PDA hydrogel evaporator

The light absorption capacity of materials determines the efficiency of the photothermal conversion. Figure 3a showed the UV-Vis-IR absorption spectrum of the hydrogel evaporator in the 200–2500 nm range alongside the standard solar radiation spectrum. The P-BC-S hydrogel exhibited extremely weak full-spectrum absorption, rendering it nearly incapable of capturing solar energy. In contrast, the P-BC-S/MXene@PDA hydrogel achieved over 87% full-spectrum absorption, with an absorption rate exceeding 92% in the 400–1500 nm range (visible-near-infrared region). This was attributed to MXene being a zero-bandgap two-dimensional conductor, where electrons could transition across a broad energy range, inherently covering UV-Vis-IR light absorption. In addition, the three-dimensional porous framework caused multiple scattering or reflection of incident light, extending its propagation path within the hydrogel and enhancing interaction with MXene@PDA as the light-absorbing component. To visually demonstrate the light absorption capability of the P-BC-S/MXene@PDA hydrogel, we simulated standard 1 sun illumination (1 $kW \cdot m^{-2}$) using a xenon lamp and monitored the hydrogel surface temperature with an infrared camera. As shown in Fig. 3c, under 1 sun irradiation, the surface temperature of the P-BC-S/MXene@PDA hydrogel rapidly increased to 49.6°C within 15 seconds and reached 66.5°C within 180 seconds, exhibiting nearly uniform temperature distribution. This indicated that MXene@PDA composites were uniformly dispersed within the hydrogel matrix, ensuring rapid and homogeneous thermal conduction throughout the material. After 3 minutes of illumination, the temperature of the P-BC-S/MXene@PDA hydrogel gradually stabilized, showing no significant change within 20 minutes. In contrast, the P-BC-S hydrogel only increased from 25°C to a maximum of 32.8°C within 20 minutes due to the lack of photothermal materials (Fig. 3b). The surface temperature variation of the P-BC-S/MXene@PDA hydrogel undergoing three illumination cycles under 1 sun illumination was displayed in Fig. 3d. After 10 min of illumination, the hydrogel surface reached 69.7°C. Upon light removal, the surface temperature decreased to 26.9°C within 10 min. Repeating this process three times, the surface temperature consistently reached approximately 68°C. This demonstrated the robust interface bonding between the MXene@PDA photothermal material and the P-BC-S scaffold, ensuring good reliability for long-term photothermal applications.

3.5 Interfacial evaporation performance of the P-BC-S/MXene@PDA hydrogel evaporator

As shown in Fig. 4a, pure water exhibited negligible mass loss in darkness. The evaporation rate of the P-BC-S hydrogel was 0.62 $kg{\cdot}m^{-2}{\cdot}h^{-1}$, while the evaporation rate of the P-BC-S/MXene@PDA hydrogel reached 1.80 $kg{\cdot}m^{-2}{\cdot}h^{-1}$. The incorporation of the photothermal material MXene@PDA composites significantly enhancesd photothermal conversion efficiency, thereby accelerating water evaporation. As solar radiation intensity increased from 0.6 to 2 sun irradiation, the water evaporation rate of the P-BC-S/MXene@PDA hydrogel markedly rose from 1.10 $kg{\cdot}m^{-2}{\cdot}h^{-1}$ to 2.74 $kg{\cdot}m^{-2}{\cdot}h^{-1}$ (Fig. 4b). The evaporation efficiency reached as high as 107.1% under 1 sun irradiation, which was attributed to MXene's plasmonic light absorption combined with efficient water transport facilitated by the porous structure (Fig. 4c). To investigate the cyclic performance of the P-BC-S/MXene@PDA hydrogel, a water cyclic evaporation test was conducted under 1 sun irradiation. The average evaporation rate over 10 consecutive cycles was 1.80 $kg{\cdot}m^{-2}{\cdot}h^{-1}$ with minimal fluctuations (Fig. 4d), indicating excellent cyclic evaporation stability and meeting the demands of long-term interfacial water evaporation applications. This evaporation rate was also higher than most of those of the evaporators reported in the literatures [2, 33–41] (the relevant evaporation rates were shown in Table S1). Purification of industrial wastewaters was an important way for harvesting fresh water. In this work, the fresh water acquisition capacity of the P-BC-S/MXene@PDA hydrogel evaporator towards wastewater containing organic dyes was investigated. Three solutions of MB, MO and RhB were prepared at an initial concentration of 30 mg/L for photo-distillation treatment. After photothermal evaporation, the collected water were all transparent liquids, and the characteristic UV absorption peaks of MB, MO, and RhB were completely eliminated by comparing the absorbance curves as well as actual images (Fig. 5d-f).

3.6 Photothermal seawater desalination performance of the P-BC-S/MXene@PDA hydrogel evaporator

The evaporation performances of the P-BC-S/MXene@PDA hydrogel evaporator in NaCl solutions with different concentrations were revealed in Fig. 5a. By calculation, the evaporation rate of this evaporator could reached 1.57 $kg{\cdot}m^{-2}{\cdot}h^{-1}$ in simulated seawater (3.5wt% NaCl solution). Even under high-salinity environment (15 wt% NaCl solution), an evaporation rate of 1.41 $kg{\cdot}m^{-2}{\cdot}h^{-1}$ solution still could be obtained. Salt resistance was a key indicator for evaluating the long-term evaporation stability of evaporators in seawater. In this study, cyclic tests were conducted in 3.5 wt% NaCl solution. After five cycles, the maximum evaporation rate loss was only 7.5%, confirming the evaporator's excellent salt-repellent properties (Fig. 5b). The robust salt resistance of the evaporator also was verified through the following experiment: NaCl particles were artificially covered on the surface of the hydrogel evaporator at the beginning of photothermal evaporation in seawater. As time progressed, the amount of NaCl on the surface of the hydrogel evaporator did not increase. On the contrary, NaCl particles increasingly disappeared and was invisible after 240 min (Fig. S6). The result indicated that sufficient water could continuously reach the surface of the evaporator through its internal channels to dissolve NaCl particles, further demonstrating the evaporator's robust salt resistance. An outdoor real seawater evaporation experiment was carried out to estimate the practicability of the evaporator under natural conditions. The

evaporation and water recipient apparatus were shown in Fig. 5c, and the daily temperature and irradiance data were presented in Fig. 5d. The maximum irradiance and temperature reached 0.9 solar intensity and 35°C, respectively. Over the 4 consecutive days, no salt accumulation was observed on the surface of the P-BC-S/MXene@PDA hydrogel evaporator (Fig. S7). From 10:00 a.m. and 16:00 p.m. in every day, the water production of the P-BC-S/MXene@PDA hydrogel evaporator was shown in Fig. 5e, the maximum water production was up to 5.642 $kg \cdot m^{-2}$ (Fig. 5e). Detection results of the ion concentrations in the collected freshwater were revealed in Fig. 5f. Metal ion concentrations decreased from 11980 (Na^+), 465 (K^+), 1250 (Mg^{2+}), and 572 (Ca^{2+}) mg/L to 5.282, 0.268, 0.154, 0.867mg/L with ion removal efficiencies of about 99% (Fig. 5f), meeting the WHO drinking water salinity standard (1000 mg/L). Above results demonstrated the significant application potential of this hydrogel evaporator in practical seawater desalination.

4. Conclusion

In summary, the P-BC-S/MXene@PDA hydrogel evaporator using BC nanofibers as “bridging agents” and MXene@PDA composites as photothermal components was designed. The as-obtained evaporator owned excellent photothermal performance, strong durability and salt resistance. The evaporation rates of 1.80 $kg \cdot m^{-2} \cdot h^{-2}$ and 1.57 $kg \cdot m^{-2} \cdot h^{-1}$ in pure water and in simulated seawater, repectively, were obtained. Meanwhile, the evaporator also exhibited its practical potential of freshwater harvesting capacity from dye sewage and seawater.

Declarations

Supporting information

Additional characterizations (TEM, XRD, FTIR, XPS, and UV-vis spectrum) of relevant samples.

Declaration of competing interest

The authors declare no competing financial interest.

Author contributions

Lei Chen: Writing-original draft and Conceptualization. Zhilong Lin and Yu Gao: Data curation. Wenqin Wang: Writing-review & editing, Project administration and Funding acquisition.

Acknowledgement

This work was supported by Natural Science Foundation of Ningbo Municipality (2024J116).

References

1. Li Y-B, Xu L, Han S-J, Liu C-H, Zhou Y, Fu M-L, Baoling Yuan (2025) Tea waste biochar hydrogel evaporator with high salt-resistance for highly efficient solar interfacial evaporation. Sep Purif Technol 361:131276. https://doi.org/10.1016/j.seppur.2024.131276
2. Xinyan Tan X, Yuan Y, Sun W, Liu J, Li (2024) Efficient solar-driven interfacial water evaporation: Construction of facilely PVA/TA/GO gel copper foam evaporator. J Environ Chem Eng 12(6):114881. https://doi.org/10.1016/j.jece.2024.114881
3. Rattan Lal (2015) World water resources and achieving water security. Agron J 107(4):1526–1532. https://doi.org/10.2134/agronj15.0045
4. Hilla Shemer R Semiat (2017) Sustainable RO desalination – Energy demand and environmental impact. Desalination 424:10–16. https://doi.org/10.1016/j.desal.2017.09.021
5. Soon-Ho, Choi (2016) On the brine re-utilization of a multi-stage flashing (MSF) desalination plant. Desalination 398:64–76. https://doi.org/10.1016/j.desal.2016.07.020
6. Shahzada Aly H, Manzoor S, Simson A, Abotaleb J, Lawler AN Mabrouk (2021) Pilot testing of a novel Multi Effect Distillation (MED) technology for seawater desalination. Desalination 519:115221. https://doi.org/10.1016/j.desal.2021.115221
7. Ihsanullah Ihsanullah MA, Atieh M, Sajid, Mazen K, Nazal (2021) Desalination and environment: A critical analysis of impacts, mitigation strategies, and greener desalination technologies. Sci Total Environ 780:146585. https://doi.org/10.1016/j.scitotenv.2021.146585
8. Liu J, Zhang S, Wang J, Qiao Lan (2025) Recent progress in solar-driven interfacial evaporation: Evaporators, condensers, applications and prospects. Desalination 597:118356. https://doi.org/10.1016/j.desal.2024.118356
9. Yuqing S, Tan X, Yuan X, Li J (2024) Solar-driven interfacial evaporation: Research advances in structural design. Chem Eng J 495:153316. https://doi.org/10.1016/j.cej.2024.153316
10. Wang J, Kong Y, Liu Z, Wang H (2023) Solar-driven interfacial evaporation: Design and application progress of structural evaporators and functional distillers. Nano Energ 108:108115. https://doi.org/10.1016/j.nanoen.2022.108115
11. Shen Du B-L, Bai Y-L, He M, Dai J-C Wan (2025) Single-stage reverse-structured solar evaporator from two to three dimensional by transparent hydrogel. Chem Eng J 524:169518. https://doi.org/10.1016/j.cej.2025.169518
12. Li J, He J, Ge J, Zhang R, Yao Y, Zhu X, Sun C, Mengnan Qu (2023) High-performance Janus evaporator based on self-healing hydrogels for salt-rejecting interfacial solar desalination. Desalination 564:116812. https://doi.org/10.1016/j.desal.2023.116812
13. Wang M, Xu G, Wu Y, Gonzales RR, Xu K, Zhao H, Wang F (2024) Engineering hydrogels towards next-generation multifunctional interfacial solar evaporators beyond seawater desalination. Chem Eng J 502:157988. https://doi.org/10.1016/j.cej.2024.157988

14. Menghan Wang J, Bai K, Shao W, Tang X, Zhao D, Lin S, Huang C, Chen Z, Ding J Ye (2021) Poly (vinyl alcohol) Hydrogels: The Old and New Functional Materials. Int J Polym Sci 12225426. https://doi.org/10.1155/2021/2225426
15. Wang H, Yang L, Yang Y (2025) A review of sodium alginate-based hydrogels: Structure, mechanisms, applications, and perspectives. Int J Biol Macromol 292:139151. https://doi.org/10.1016/j.ijbiomac.2024.139151
16. Sui J, Chen X, Li Y, Peng W, Zhang F, Xiaobin, Fan (2021) MXene derivatives: synthesis and applications in energy convention and storage. RSC Adv 11:16065–16082. https://doi.org/10.1039/d0ra10018h
17. Siddappa A, Patil, Kostiantyn O, Marichev SA, Patil A Bugarin (2023) Advances in the synthesis and applications of 2D MXene-metal nanomaterials. Surf Interfaces 38:102873. https://doi.org/10.1016/j.surfin.2023.102873
18. Xu D, Li Z, Li L, Wang J (2020) Insights into the Photothermal Conversion of 2D MXene Nanomaterials: Synthesis, Mechanism, and Applications. Adv Funct Mater 30(47):2000712. https://doi.org/10.1002/adfm.202000712
19. Zhilong Lin Y, Gao L, Chen W, Wang T, Chen (2025) Design and fabrication of PVA/SA/MXene@TA-Fe hydrogel as an efficient solar evaporator for desalination. J Environ Chem Eng 13(5):117584. https://doi.org/10.1016/j.jece.2025.117584
20. Li S, Liu J, Li C, Fang X, Xin Wang L, Tian Z-Z, Yu X, Li (2024) Robust and Antifouling Composite Hydrogels Enhanced by Directional Freeze-Casting and Salting-Out for Highly Efficient Solar Evaporation. ACS Appl Mater Interfaces 16:66560–66570. https://doi.org/10.1021/acsami.4c17304
21. Tian Wang M, Li H, Xu X, Wang M, Jia X, Hou S, Gao Q, Liu Q, Yang M, Tian L, Qu Z, Song X, Wu L, Wang X, Zhang (2024) MXene Sediment-Based Poly (vinyl alcohol)/Sodium Alginate Aerogel Evaporator with Vertically Aligned Channels for Highly Efficient Solar Steam Generation. Nano-Micro Lett 16:220. https://doi.org/10.1007/s40820-024-01433-1
22. Rojas Oviedo I, Noguéz Méndez NA, Gómez Gómez MP, Cárdenas Rodríguez H, Rubio A, Martínez (2008) Design of a Physical and Nontoxic Crosslinked Poly (Vinyl Alcohol) Hydrogel. Int J Polym Mater 57:1095–1103. https://doi.org/10.1080/00914030802341661
23. Li W, Wu Z, Zhao J, Jiang M, Yuan L, Guo Y, Li S, Xie LHX, Zhang Y, Tao G, Rui Cai (2023) Fabrication of dual physically cross-linked polyvinyl alcohol/agar hydrogels with mechanical stability and antibacterial activity for wound healing. Int J Biol Macromol 247:125652. https://doi.org/10.1016/j.ijbiomac.2023.125652
24. Wang M, Li J, Li W, Du Z, Song Qin (2018) Preparation and characterization of novel poly (vinyl alcohol)/collagen double-network hydrogels. Int J Biol Macromol 118:41–48. https://doi.org/10.1016/j.ijbiomac.2018.05.200
25. Razium A, Soomro P, Zhang B, Wei FY, Xu B (2023) Progression in the Oxidation Stability of MXenes. Nano-Micro Lett 15(1):108. https://doi.org/10.1007/s40820-023-01069-7

26. Xi Z, Wang F, Yu Y, Guo R, You X, Xiang X, Niu XFY, Wang X, Feng X, Lin Chen (2025) Muti-network active aerogel based on PVA, bacterial cellulose, and sodium alginate: Characterization, kinetics studies, and application for mutton preservation. Food Hydrocolloids 165:111033. https://doi.org/10.1016/j.foodhyd.2024.111033
27. Fu Y, Yang L, Zhang J, Duan JHG, Liu X, Li Y, Zhipeng Gu (2021) Polydopamine antibacterial materials. Mater Horiz 8:1618–1633. https://doi.org/10.1039/d0mh01985b
28. Zhang F, Zou Yi-liang, Luo R, Yang Jing-hui, Sun De-xiang, Zhang N, Wang Y (2025) Synchronously enhanced breakdown strength and energy storage performance of cellulose acetate sandwich-structured composite films utilizing MXene@PDA nanosheets. Polymer 335:128799. https://doi.org/10.1016/j.polymer.2025.128799
29. Xiangxiang Shi Z, Yu Z, Liu N, Cao L, Zhu Y, Liu K, Zhao T, Shi L, Yin Z Fan (2024) Scalable, High-Yield Monolayer MXene Preparation from Multilayer MXene for Many Applications. Angew Chem Int Ed 64(6):e202418420. https://doi.org/10.1002/anie.202418420
30. Guo Y, Baschieri A, Mollica F, Valgimigli L, Cedrowski J, Litwinienko G, Riccardo Amorati (2021) Hydrogen Atom Transfer from HOO· to ortho-Quinones Explains the Antioxidant Activity of Polydopamine. Angew Chem Int Ed 60(28):15220–15224. https://doi.org/10.1002/anie.202101033
31. He X, Wu J, Chen Y, Zhang L, Xinxin Sheng (2022) A trace amount of MXene@PDA nanosheets for low-temperature zinc phosphating coatings with superb corrosion resistance. Appl Surf Sci 603:154455. https://doi.org/10.1016/j.apsusc.2022.154455
32. Chen S, Xu J, Shi M, Yu Y, Xu Q, Duan X, Gao Y, Lu L (2021) Polydopamine bridged MXene and NH2-MWCNTs nanohybrid for high-performance electrochemical sensing of acetaminophen. Appl Surf Sci 570:151149. https://doi.org/10.1016/j.apsusc.2021.151149
33. Mingfeng Dong Z, Zhu Y, Dai D, Yang T, Zhang F Qiu (2025) A bilayer hydrogel evaporator with vertical channel for desalination applications. J Water Process Eng 78:108846. https://doi.org/10.1016/j.jwpe.2025.108846
34. Hongwei Jian Q, Qi W, Wang D Yu (2021) A Janus porous carbon nanotubes/poly (vinyl alcohol) composite evaporator for efficient solar-driven interfacial water evaporation. Sep Purif Technol 264:118459. https://doi.org/10.1016/j.seppur.2021.118459
35. Cao Y, Liang L, Zhang Z, Tang Y, Zhang Y, Dong S, Liu H, Lang Liu (2025) Dual Cross-Linking Coal Tar-Derived Phenolic Resin Porous Carbon-Based Hydrogel Solar Evaporators for Efficient Wastewater Purification. Langmuir 41(12):8192–8201. https://doi.org/10.1021/acs.langmuir.4c05279
36. Zuoyu Wang N, Jin L, Lu S, Ao Y, Zhang S, Qi T Jia (2025) Highly efficient solar-thermal thermoresponsive hydrogel based on a fullerene derivative for water purification and energy harvesting. J Mater Chem C 13(21):10817–10824. https://doi.org/10.1039/d5tc00795j
37. Hongxia Cao D, Wang Z, Sun Y Zhu (2022) In Situ Carbonized Polyvinyl Alcohol (PVA) Sponge by a Dehydration Reaction for Solar-Driven Interfacial Evaporation. Sustainability 14(17):10945. https://doi.org/10.3390/su141710945

38. Zhang Z, Liang L, Jia Z, Tang Y, Liu L, Xu Y, Dong S, Zhang Y, Zhou Y, Chunmei Ma (2025) Non-symmetric evaporator by polyvinyl alcohol encapsulated coal tar pitch-based carbon and sponge foam for solar-driven interfacial evaporation. Sep Purif Technol 374:133564. https://doi.org/10.1016/j.seppur.2025.133564
39. Lian Song X-F, Zhang Z, Wang T, Zheng J Yao (2021) Fe3O4/polyvinyl alcohol decorated delignified wood evaporator for continuous solar steam generation. Desalination 507:115024. https://doi.org/10.1016/j.desal.2021.115024
40. Anqi Shen J, Tang Y, Shao J, Chen Y, Liu D, Wang H, Zhi H, Liu G Xue (2023) Architecting the Water State of Polypyrrole/Polyvinyl Alochol-Wood Evaporator to Enhance Water Yield in Multistage Solar Stiller. Solar RRL 7(5):2200915. https://doi.org/10.1002/solr.202200915
41. Jing Li L, Yan X, Li W, Song Y, Li (2022) Porous polyvinyl alcohol/biochar hydrogel induced high yield solar steam generation and sustainable desalination. J Environ Chem Eng 10(3):107690. https://doi.org/10.1016/j.jece.2022.107690

Figures

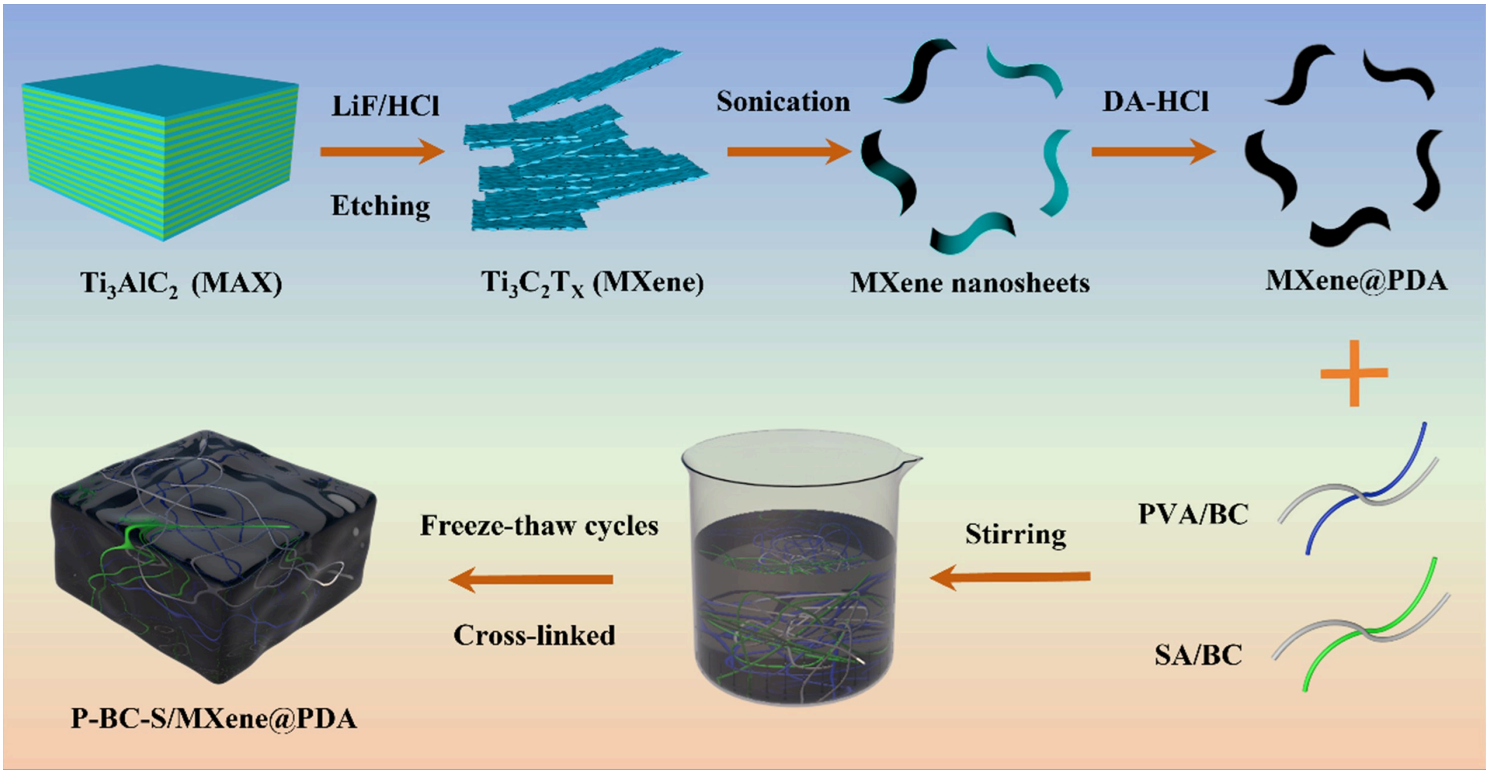


Figure 1

Schematic illustration of the preparation process of the P-BC-S/MXene@PDA hydrogel.

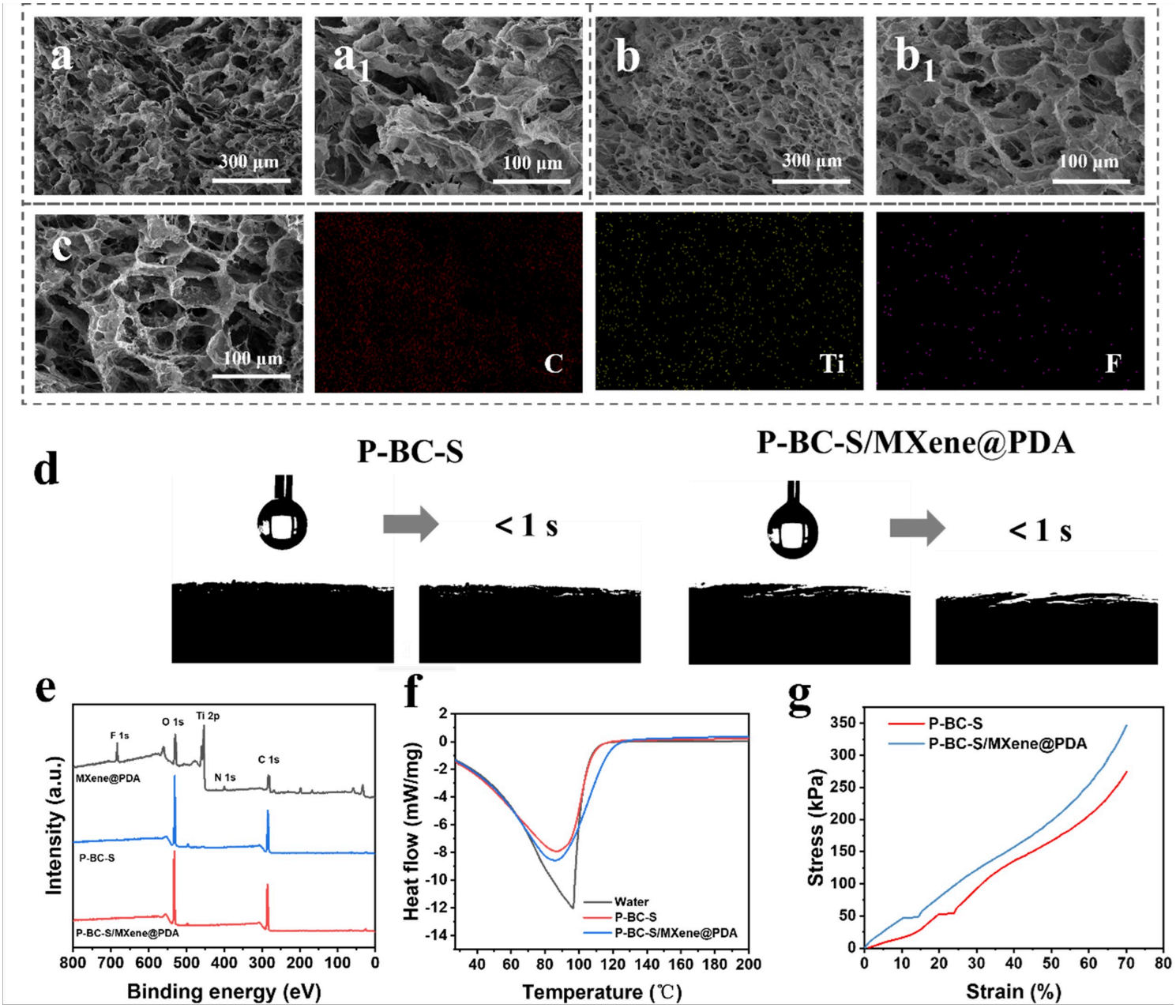


Figure 2

SEM images of the P-BC-S hydrogel (a, a_1) and P-BC-S/MXene@PDA hydrogel (b, b_1). SEM image and corresponding EDS spectra of the P-BC-S/MXene@PDA hydrogel (c). The hydrophilic properties of the hydrogels (d). XPS spectra of MXene@PDA composites, P-BC-S, and P-BC-S/MXene@PDA hydrogels (e). DSC curves of pure water, P-BC-S, and P-BC-S/MXene@PDA hydrogel (f). Compressive stress-strain curves of the samples (g).

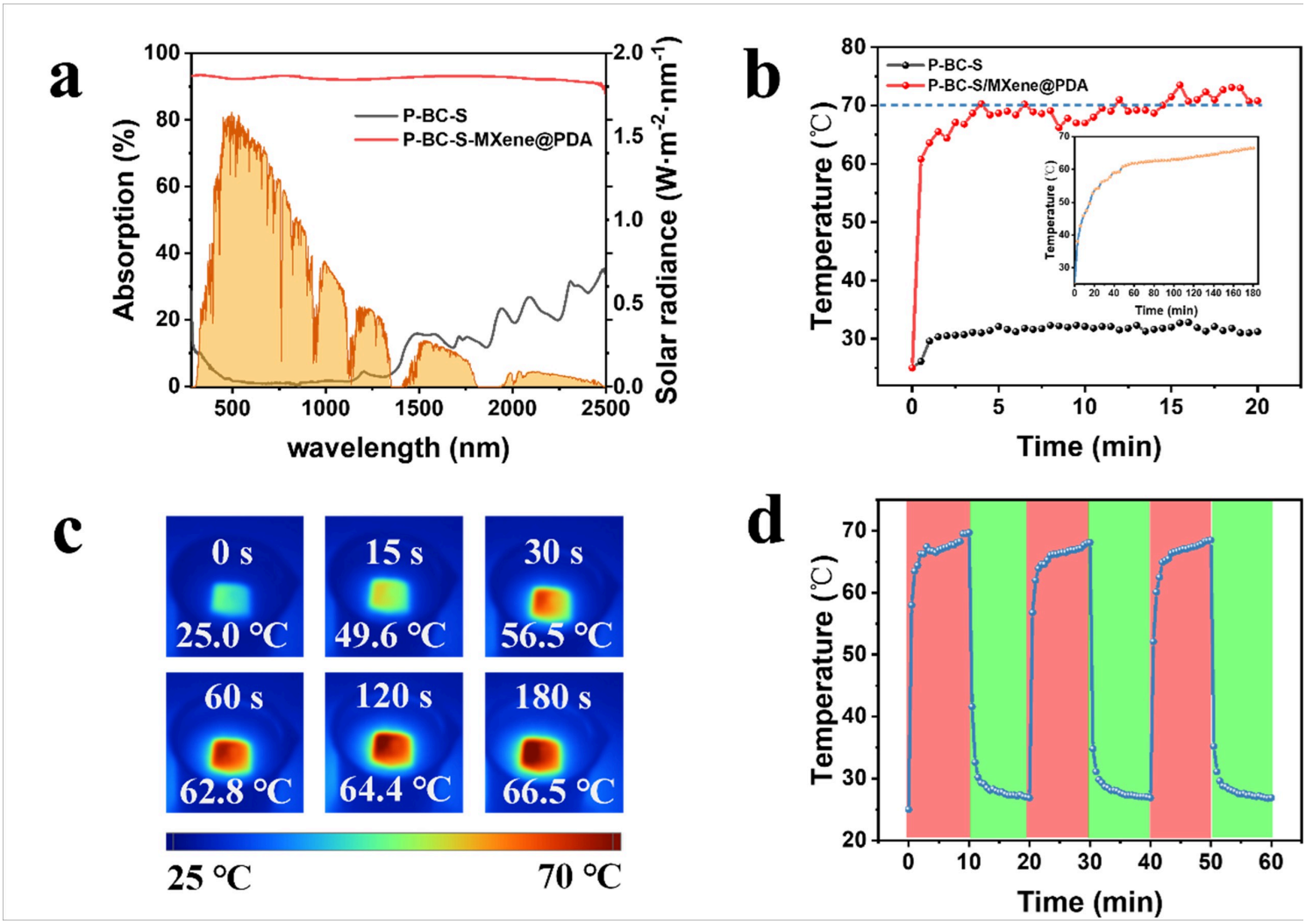


Figure 3

UV-Vis-IR spectra of the hydrogel in the 200-2500 nm range (a). Temperature rise curve of the hydrogel surface under 1 sun irradiation (b). Infrared thermal imaging of the temperature rise on the surface of P-BC-S/MXene@PDA hydrogel under 1 sun irradiation (c). Surface temperature variation of P-BC-S/MXene@PDA hydrogel during light cycles under 1 sun illumination (one cycle consists of 10 min illumination followed by 10 min removal of light source) (d).

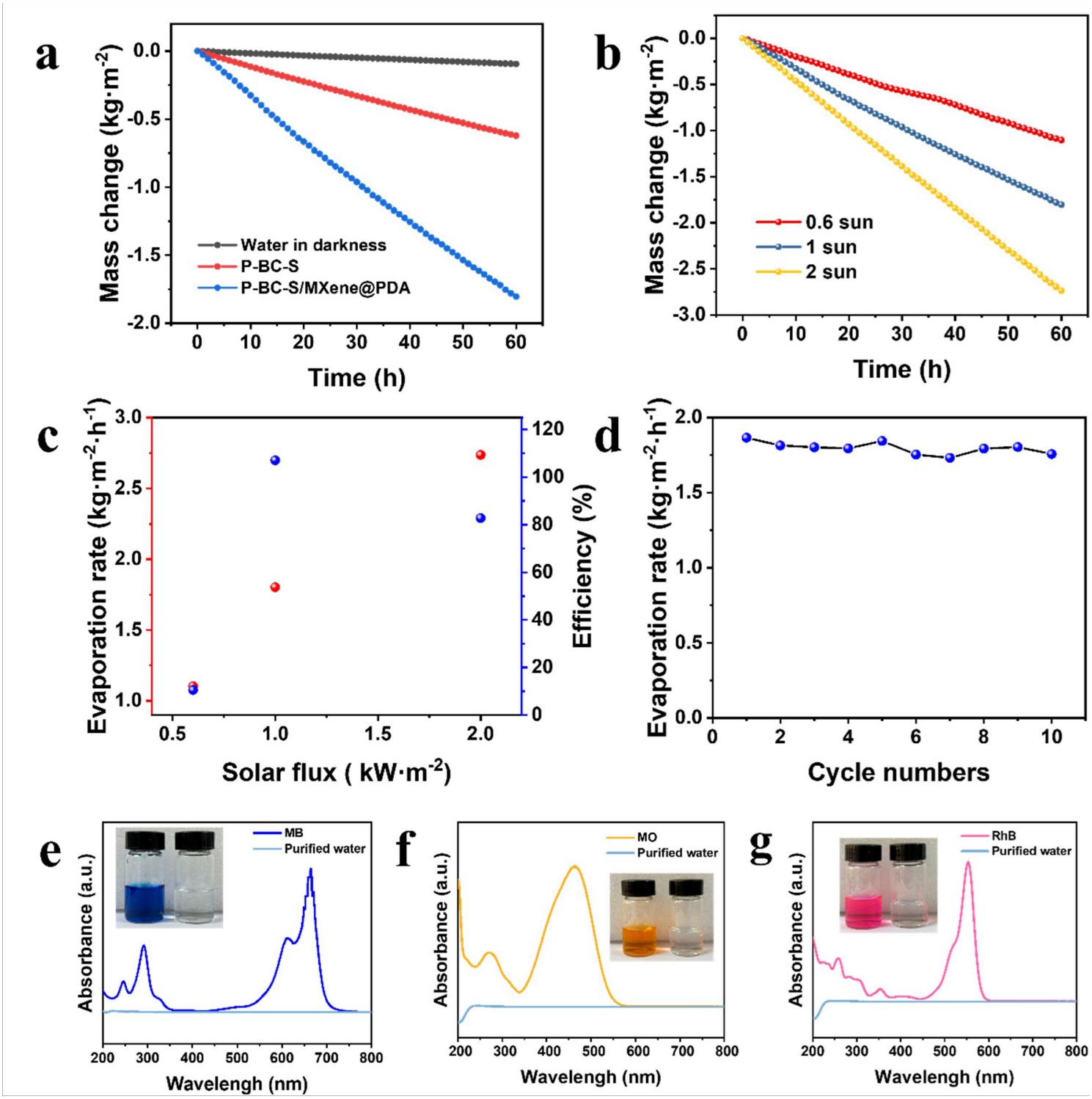


Figure 4

Evaporation rate of hydrogel under 1 sun irradiation (a). Evaporation rates under different solar irradiance levels (b). Evaporation rates and evaporation efficiencies under varying solar irradiance conditions (c). Pure water cyclic evaporation performance of P-BC-S/MXene@PDA hydrogel under 1 sun irradiation (d). UV-vis absorption spectra and digital images before and after organic pollutant evaporation (e-g).

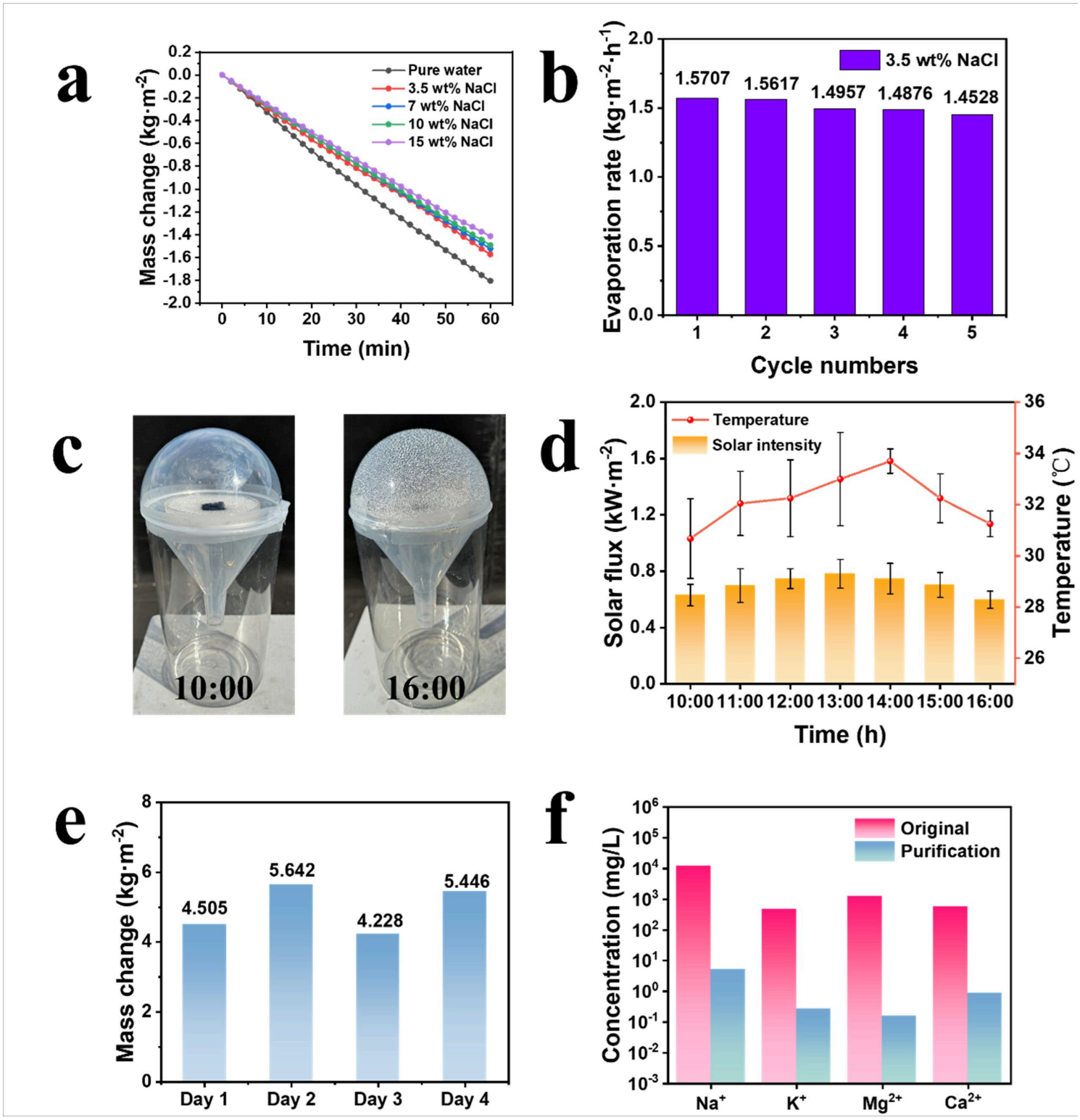


Figure 5

Water evaporation performance testing of NaCl solutions at different mass fractions (a). Cyclic testing of the evaporation performance in 3.5 wt% NaCl solution (b). Home-made evaporation apparatus in outdoor photothermal evaporation experiment (c). The variations of temperature and light intensity in outdoor (d) (Zhenhai District, Ningbo, October 10, 2025). Daily total water production (e). Comparison of ion concentrations between seawater and evaporatived freshwater (f).

Supplementary Files

This is a list of supplementary files associated with this preprint. Click to download.

- SupportingInformation.docx